Journal of Alloys and Compounds 785 (2019) 925–931

Contents lists available at ScienceDirect

Journal of Alloys and Compounds

journal homepage: http://www.elsevier.com/locate/jalcom

Improved reaction kinetics and reserved spacial structure of Fe_3C-SnO_2@void@C toward high-performance lithium storage

Weijian Huang [a, b, c], Lan Chen [a, b, c], Yue Chen [a, b, c], Mingzhong Zou [a, b], Feng Qian [a, b, c], Jiaxin Li [a, b, c, *], Zhigao Huang [a, b, c, **]

[a] College of Physics and Energy, Fujian Normal University, Fujian Provincial Key Laboratory of Quantum Manipulation and New Energy Materials, Fuzhou, 350117, China
[b] Fujian Provincial Collaborative Innovation Center for Optoelectronic Semiconductors and Efficient Devices, Xiamen, 361005, China
[c] Fujian Provincial Key Laboratory of Nanomaterials, Fujian Institute of Research on the Structure of Matter, Chinese Academy of Sciences, Fuzhou, Fujian, 350002, China

ARTICLE INFO

Article history:
Received 24 November 2018
Received in revised form
28 December 2018
Accepted 31 December 2018
Available online 3 January 2019

Keywords:
Lithium-ion batteries
Fe_3C-SnO_2@void@C anodes
Capacity contribution
Battery performance

ABSTRACT

Lithium ion battery (LIB) anode of Fe_3C modified SnO_2@void@C has been rationally prepared *via* wet chemical method coupled with vapor-phase treatment. In this architecture, the Fe_3C modification and carbon protective shell can both improve the electrical conductance, the inner void space can tolerate the volume expansion/shrinkage of SnO_2, and the outer carbon protective shell can hamper aggregation of active materials. These composites have been used as LIB anodes, delivering good LIB performance with a capacity of ~580 mAh g^{-1} cycling after 350 cycles at 800 mA g^{-1}, good rate performance with a capacity retention of over 728 mAh g^{-1} for 65 cycles. Kinetic analysis reveals that the improved LIB performance of Fe_3C modified composites could be also associated with the contribution of capacitive charge. In addition, the related redox mechanism has been investigated in detail. Thus, this work supplied a promising route to prepare the high-performance LIB anodes with improved coulombic efficiency, large reversible electrochemical capacity and long cycling life.

1. Introduction

The ever-increasing demand for lithium-ion batteries (LIBs) with higher capacity and faster cycling rates underscores the need for high-performance electrode materials [1–4]. As a promising anode material for LIBs, SnO_2 possesses relative high theoretical specific capacity (782–1493 mAh g^{-1}), being several times larger than that of 372 mAh g^{-1} for commercial graphite [5–7]. However, SnO_2 anode still face the obstacle of its huge volume expansion (~230%), poor electronic conductivity and the corresponding caused problems upon lithiation/delithiation process [8,9]. Enormous efforts have been devoted to overcoming these obstacles and further improving the LIB performance of SnO_2 anodes *via* various strategies [5–9].

In order to solve the problem of volume expansion during cycling process, different carbonaceous materials including carbon nanofibers [7], carbon nanotubes [10], carbon nanohorns [11] and graphene [12], have been usually utilized as carriers to sustain SnO_2 anodes. The supporting strategy may somewhat reduce the volume changes and suppress the pulverization. After long lithiation/delithiation process, the repeated unbalanced strain during expansion/shrinkage would inevitably cause the final pulverization, thereby leading to the failure of SnO_2 anode. Furthermore, the passivated solid electrolyte interphase (SEI) films can continuously rupture and re-form caused by the successive volume change [13,14]. This result could deplete the electrolyte and lead to high resistance for lithium ions transport, often resulting to the quick die of batteries. According to the previous reports [15–19], carbon coating combined with reserved spacial structure, such as hollow nanostructure [16–19], yolk-shell nanostructure [16,17] and coaxial cable nanostructure [18,19], has been regarded as one of the most feasible strategy. Herein, the yolk-shell architecture could not only offer void space to tolerate the volume expansion of the active materials, but also stabilize SEI films through its stable outer carbon

* Corresponding author. College of Physics and Energy, Fujian Normal University, Fujian Provincial Key Laboratory of Quantum Manipulation and New Energy Materials, Fuzhou, 350117, China.
** Corresponding author. College of Physics and Energy, Fujian Normal University, Fujian Provincial Key Laboratory of Quantum Manipulation and New Energy Materials, Fuzhou, 350117, China.
E-mail addresses: ljx0721@qq.com (J. Li), zghuang@fjnu.edu.cn (Z. Huang).

https://doi.org/10.1016/j.jallcom.2018.12.388
0925-8388/

shell [19,20]. However, being similar to other reports, our group previously designed a yolk-shell Fe_3O_4@C anodes, and revealed that the carbon shell carbonized from glucose and the relative small reserved space cannot effectively maintain the original appearance [21]. Therefore, building a stable carbon shell with ample space to stabilize the yolk-shell SnO_2-based anodes is desirable.

As a semiconductor material, another problem encountered by SnO_2 anodes is poor conductance. Similar to other oxide anodes, this character would lead to the electrode polarization and the further attenuation of cyclic efficiency, meaning the waste of energy [22,23]. As the above discussion, various carbonaceous materials including carbon coating have been used to improve conductance of SnO_2 composites. For SnO_2, the cycling occurred in LIBs often contains the partial reversible conversion reaction 1 of "$SnO_2 + 4Li^+ + 4e^- \rightarrow Sn + 2Li_2O$" and the highly reversible alloy reaction 2 of "$xLi^+ + Sn + xe^- \leftrightarrow Lix\,Sn\ (0 \leq x \leq 4.4)$". It is reported that SnO_2 anodes can achieve both reactions 1 and 2 only with good conductance [23,24]. Especially, the related reports pointed out that the carbon shell combined with metal particles or metal carbide particles would stabilize the SEI films, and ulteriorly promote the cycling coulombic efficiency and their reversible Li storage [25,26]. Besides, hollow carbon-coating shell with large specific surface and good conductance could possibly exhibit pseudocapacitive behavior, simultaneously achieving both large power density and high energy output [27,28]. Investigating the related redox behavior from capacitive contribution is important to reveal the enhanced mechanism for LIB performance. Nevertheless, to design coaxial cable structures is relative complicated, and the carbon-coating shell should be rationally controlled to optimize the LIB performance.

Here, we prepared anode composite of SnO_2@void@C with Fe_3C modification and used as lithium battery anode. These composites can deliver good LIB performance with large reversible capacity, good rate capacity and stable cycling life. The related redox mechanism for the enhanced LIB performance has been investigated in detail.

2. Experimental

2.1. Synthesis of materials

In this paper, all analytical grade chemicals were used as received. Firstly, the SnO_2 spheres were prepared as our previous work [29]. And then, 4.0 ml ethanol mixed with 0.15 ml TEOS was added drop wise into the solution with 100 mg SnO_2 spheres, 10 ml deionized H_2O, 70 ml ethanol and 3.14 ml NH_4OH under vigorous stirring for 8.0 h. Thus, the composite of SnO_2@SiO_2 can be obtained. The process of carbon shell coating is described as below: SnO_2@SiO_2 composites were firstly dispersed in 40 ml deionized H_2O for 1.0 h, 0.05 ml NH_4OH and 0.5 ml 0.01 mol L^{-1} CTAB were added in the above-solution for stirring 0.5 h, and then 25 mg resorcinol (R) and 0.035 ml formaldehyde (F) were added for additional stirring 16.0 h at room temperature for obtaining SnO_2@SiO_2@RF. The SnO_2@SiO_2@RF precursors subsequent calcinated at 550 °C under Ar gas. The SiO_2 coated layer was etched away with 100 ml 2M NaOH solution for 50 h at 60 °C to obtain the yolk-shell SnO_2@void@C sample. At last, 15 mg ferrocene and 45 mg SnO_2@void@C were uniformly mixed and placed in vacuum quartz glass tube. The mixture was calcinated at 500 °C for 3 h to obtain the Fe_3C modified yolk-shell SnO_2@void@C sample.

2.2. Material characterization

The Scanning electron microscopy (SEM, JSM 6700F), transmission electron microscopy (TEM, Tecnai G2 F20), high-resolution TEM (Tecnai G2 F20), X-ray diffraction (XRD, RIGAKU SCXmini), Autosorb-iQ2-XR (Quantachrome Instruments) and thermogravimetric analysis (TGA, Rigaku-TD-TDA) were utilized to analyze the samples of SnO_2 nanosphere, SnO_2@SiO_2@C, SnO_2@void@C and Fe_3C-SnO_2@void@C. The surface potential of the electrodes was characterized by Kelvin probe atomic force microscopy (KPAFM) (Bruker dimension ICON, Germany), which measured the strength of the electrostatic forces between the conductive probe and the sample.

2.3. Electrode assembly and electrochemical measurements

The LIB properties for obtained composites were evaluated *via* coin-type cells. A homogeneous slurry consisting of active material (80 wt%), carbon black (10 wt%) and polymer binder of sodium carboxymethyl cellulose binder (10 wt%) were pasted on the current collector and dried at 80 °C in a vacuum oven for overnight for forming the working electrodes. The test cells were assembled with working electrode, counter electrode of lithium metal sheet and the injecting electrolyte contained with 1.0 M $LiPF_6$ in EC/EMC/DMC (1: 1: 1 by volume). Herein, cyclic voltammetry (CV) tested with the potential range from 0.05 to 3.00 V under varied scan rates of 0.1–10 mV s^{-1}, and electrochemical impedance spectrum (EIS) operated by applying an ac voltage of 5 mV over the frequency range from 1 mHz to 100 kHz, were performed utilizing Electrochemical Workstation (CHI660D). Meanwhile, LAND 2001A was used to test the LIB cycling performance for the assembled cells.

3. Results and discussion

Fig. 1 presented the schematic illustration on the synthesis of various SnO_2 nanostructures. The uniform SnO_2 nanospheres were fabricated *via* a simple hydrothermal reaction. The SiO_2 layer and carbon coating shell have been gradually attached on SnO_2 through hydrolysis of TEOS, co-coagulation of SiO_2 and RF resin, carbonization of RF and subsequent calcination treatment [30]. The yolk-shell SnO_2@void@C can be obtained after the SiO_2 middle layer has been etched away by NaOH. And last, the vapor-phase treatment was employed to achieve the Fe_3C modification.

The XRD patterns for SnO_2@void@C and Fe_3C-SnO_2@void@C samples are shown in Fig. 2a. The sharp and well-defined diffraction peaks for SnO_2 components from these two samples can be identified and indexed to the tetragonal rutile SnO_2 phase (JCPDS

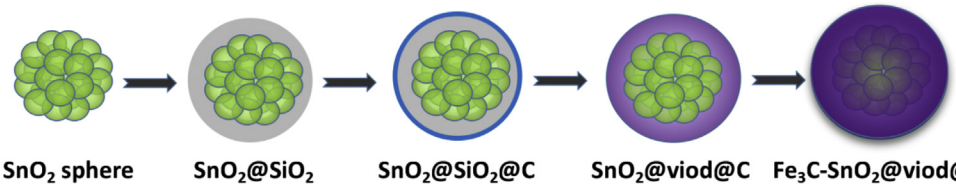

Fig. 1. Schematic illustration for the synthesis of various SnO_2 nanostructures: SnO_2 nanosphere, SnO_2@SiO_2@C, SnO_2@void@C and Fe_3C-SnO_2@void@C.

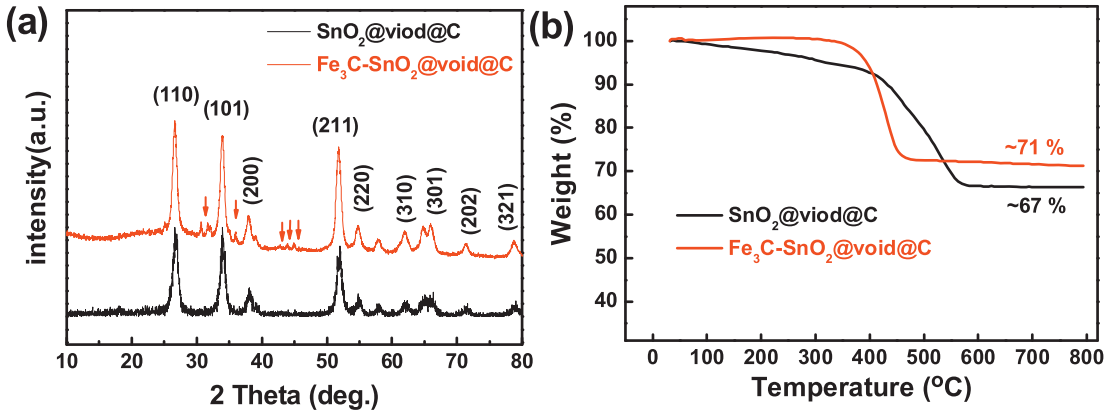

Fig. 2. (a) XRD patterns and (b) TGA of SnO_2@void@C and Fe_3C-SnO_2@void@C.

no. 41-1445) [29]. Herein, the weak peaks around 26° corresponding to the carbon shell layer can be found in Fig. 2. By comparing two XRD patterns, the peaks marked with red asterisks existed in Fe_3C-SnO_2@void@C sample, which were ascribed to Fe_3C crystalline phase (JCPDS no. 89-2867) [29]. This result revealed that the Fc precursors have been converted to Fe_3C and modified SnO_2@void@C composite. In order to confirm the element distribution of Fe_3C adding in Fe_3C-SnO_2@void@C sample, the line scan EDS element analysis was carried out and shown in Fig. S1. Combined with XRD pattern, this result prove the existence the Fe_3C adding, which has been incorporated uniformly in SnO_2@void@C. Meanwhile, the TGA result presented in Fig. 2b show that the content of SnO_2 in SnO_2@void@C composite is about 67.0 *wt%*, and that of carbon shell and Fe_3C in Fe_3C-SnO_2@void@C are 31.0 wt% and 6.0 *wt%*, respectively.

The morphology of SnO_2@void@C and Fe_3C-SnO_2@void@C samples were examined *via* SEM. From Fig. 3, the SnO_2@void@C have an average particle size of 120 ± 10 nm, being larger than that of 90 ± 10 nm for pristine SnO_2 spheres. The semitransparent carbon shell can also be observed clearly. Meanwhile, it can be observed from Figs. S2a and b that SnO_2@SiO_2 exhibit homogeneous sphere-structure with the diameter of ~120 nm, being larger than that of SnO_2 without SiO_2 coating. In addition, the pristine

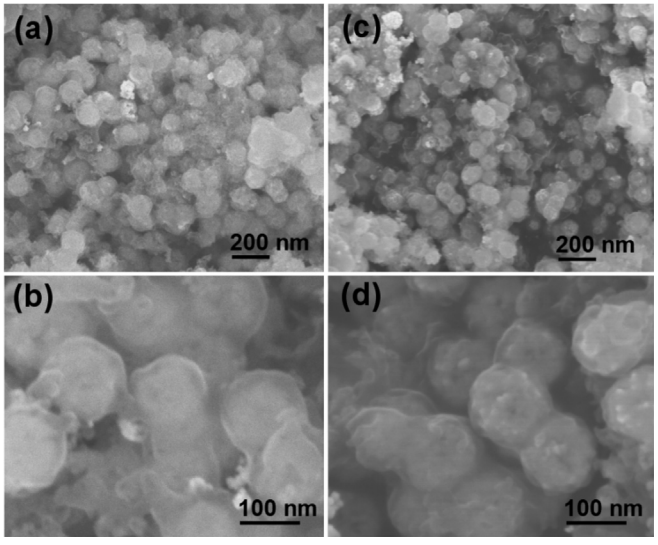

Fig. 3. SEM and magnified SEM images of (a–b) SnO_2@void@C and (c–d) Fe_3C-SnO_2@void@C.

SnO_2 spheres shown in Figs. S2c and d are made up of ~10 nm nanoparticles, exhibiting a crude porous structure. As show in Fig. 3c and d, the Fe_3C-SnO_2@void@C sample maintains its original core-shell structure, implying that the Fe_3C has been uniformly modified with the SnO_2@void@C sample. This phenomenon is similar to our previous report [25]. The main volume ratio of total carbon protective shell and SnO_2 sphere can be calculated to be about 2.3–3.0 as counted in Fig. S3, indicating sufficient inner-space for SnO_2 to overcome its volumetric change without rupturing the core-shell structure. And obtain the good LIB performance during cycling can be expected. In fact, keeping a stable carbon shell to ensure SEI stability and protect the active material from pulverization is important for SnO_2 anodes. Our group previously designed a similar yolk-shell SnO_2@C anodes, revealing that unreserved space cannot effectively maintain as original appearance [29].

In addition, the TEM and HR-TEM were used to evaluate their crystal structures and carbon shell of SnO_2@void@C and Fe_3C-SnO_2@void@C samples as shown in Fig. 4. It is found that all SnO_2 spheres are embedded well in the protective carbon shell with a thickness of ~10 nm. Detected from HR-TEM, the well-resolved d-spacing of the SnO_2 (110) and Fe_3C (031) crystal plane are 0.33 and 0.20 nm. The SAED measurement was also provided to investigate detailed crystal information about these two samples (Fig. 4g and h). The corresponding diffraction rings of (110), (101), (211) and (301) planes for SnO_2 and the (031) and (232) planes for Fe_3C are obviously distinguished [25,29].

Fig. 5a and b deliver the discharge/charge (D/C) curves of SnO_2@void@C and Fe_3C-SnO_2@void@C electrodes tested at a current density of 200 mAh g^{-1} between the voltage range of 0.05–3.00 V. As presented in figures, the D/C curves consisted of plateau regions are consistent with the redox reactions. The SnO_2@void@C Fe_3C-SnO_2@void@C samples deliver the 1st D/C capacities of 820/1443 and 888/1408 mAh g^{-1}, corresponding to initial Coulombic efficiency of 56.7% and 63.1%, respectively. The initial capacity loss is mainly caused by the formation of SEI films and the possible consumption of electrolyte decomposition. Being similar to other reports, the Fe_3C adding can promote the first Coulombic efficiency for those composites, due to such adding could reduce some SEI components and release some reversible electrochemical capacities. In addition, the LIB performance for such void structure with Fe_3C modification is slightly better than our previous report on SnO_2 anodes [29]. To further understand the redox reactions, the differential capacity versus voltage (dQ/dV) curves of the first two cycles for SnO_2@void@C and Fe_3C-SnO_2@-void@C samples were correspondingly revealed in Fig. 5c and d. In the 1st cathodic process, the strong reductive peak appearing at

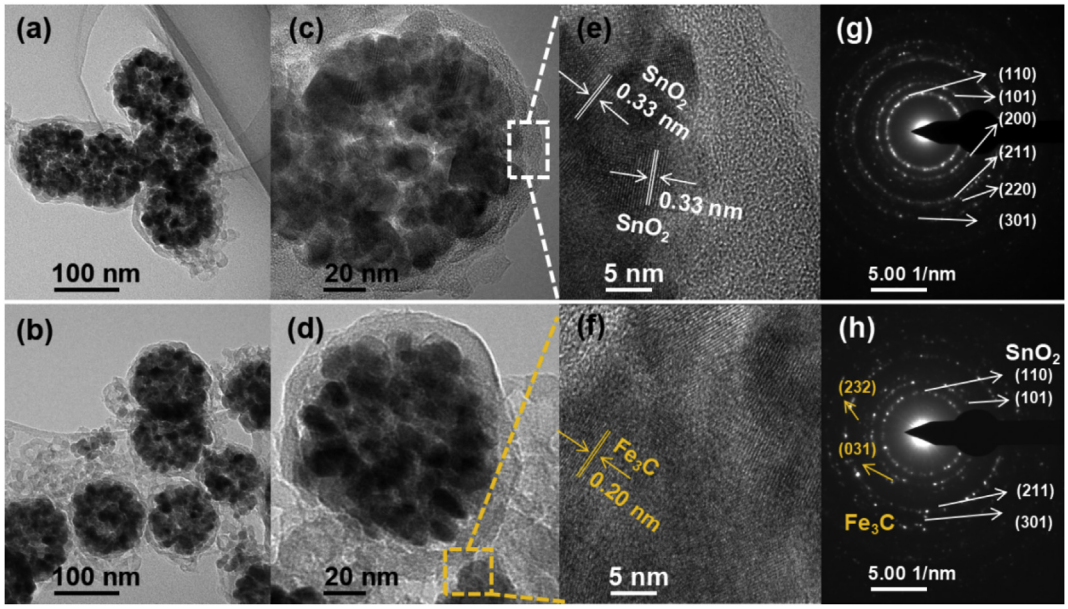

Fig. 4. TEM, magnified TEM, HR-TEM images and the corresponding SAED pattern of (a, c, e and g) SnO_2@void@C, (b, d, f and h) Fe_3C-SnO_2@void@C.

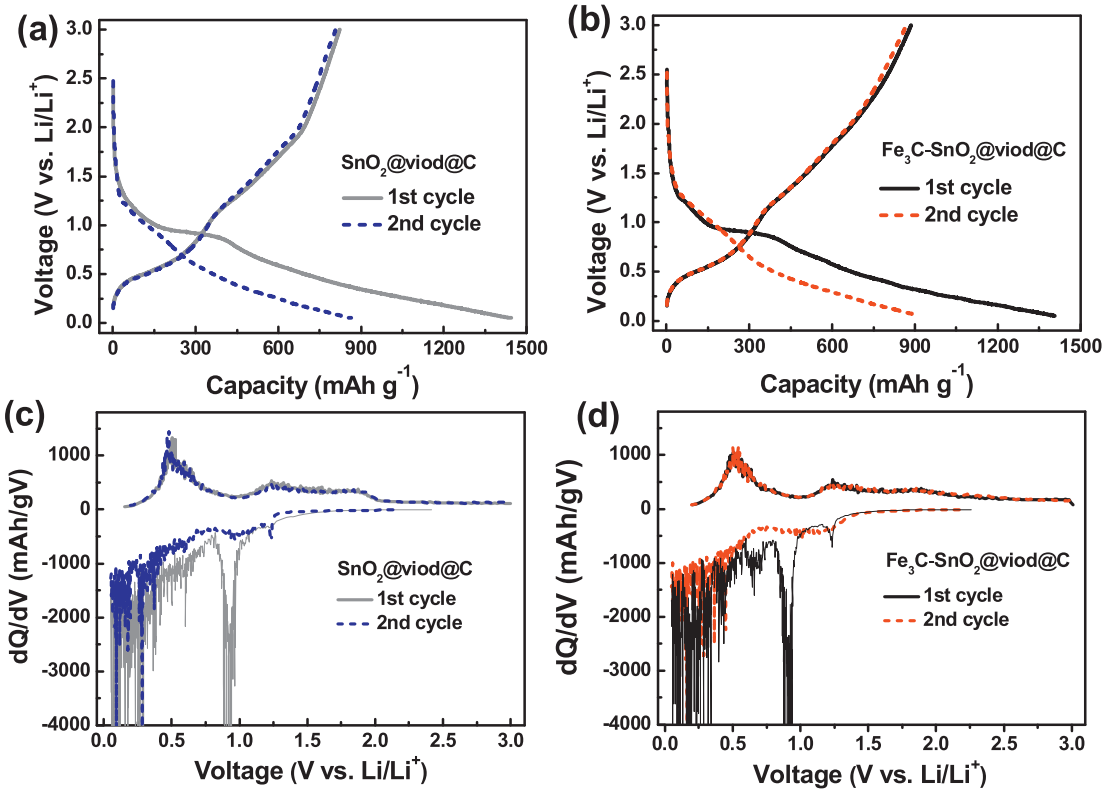

Fig. 5. (a,b) Discharge/charge voltage profiles of the SnO_2@void@C and Fe_3C-SnO_2@void@C; (c,d) differential capacity versus voltage plots of the SnO_2@void@C and Fe_3C-SnO_2@void@C corresponding to the first two cycles.

about 0.85 V and the following broad peak extending to 0.05 V are ascribed to the generation of SEI film layer and the reduction of SnO_2 to metallic Sn, and the formation of a Li-Sn alloy, respectively. In subsequent oxidation process, the peaks at ~0.55 and 1.25 V correspond to the de-alloying reaction, together with the oxidation of Sn to Sn^{4+}. It is noted that the 1st sharp peaks at ~0.85 V disappear in the following cycles for two electrodes caused by the irreversible transformation of the SEI film. Furthermore, both of dQ/dV curves after the 1st cycle overlap considerably well, therefore delivering stable LIB cycling performance. The following cycling D/C capacities reveal that the Fe_3C-SnO_2@void@C sample can possess a better LIB performance than that without Fe_3C modification.

For further comparison, the LIB cyclic performance of SnO_2@-void@C and Fe_3C-SnO_2@void@C electrodes tested at different

current densities is displayed in Fig. 6. Tested at 200 mA g^{-1}, the reversible capacity for Fe_3C-SnO_2@void@C retains at ~760 mAh g^{-1} after 50 cycles, in contrast the SnO_2@void@C only possess a low capacity of ~710 mAh g^{-1}. From Fig. 6a, the calculated Coulombic efficiency for SnO_2@void@C and Fe_3C-SnO_2@void@C electrodes increases quickly after the first several cycles, reaching up to ~98.0% and ~99.0%, respectively. Fig. 6b displays the comparison of rate performance of SnO_2@void@C and Fe_3C-SnO_2@void@C anodes tested by adjusting the current density. A better LIB rate performance also appears in Fe_3C-SnO_2@void@C electrode, providing reversible capacities of 780, 710, 672, 638 and 601 mAh g^{-1} at 200, 400, 600, 800 and 1000 mA g^{-1}, respectively. When the current density is directly turned back to 200 mA g^{-1}, the reversible capacity of 728 mAh g^{-1} can be remained for 65 cycles, much better than 600 mAh g^{-1} of SnO_2@void@C electrode. Apparently, the Fe_3C-SnO_2@void@C deliver an obviously enhanced LIB performance including reversible capacity, cycling life and cycling efficiency, which might be due to the stable SEI film formation and improved conductivity from Fe_3C modification (as shown in Figs. S4~6). Herein, the physical intrinsic conductivity is important to these samples. The KPFM and EIS results suggest that the electrons require lower energy to escape from the Fe_3C-SnO_2@void@C electrode compared with the SnO_2@void@C electrode, which can deduce Fe_3C-SnO_2@void@C possess better electric conductivity. Undoubtedly, the cycling performance of SnO_2@void@C and Fe_3C-SnO_2@void@C electrodes is much better than that of pure SnO_2 electrodes as shown in Fig. S7. In addition, the tested long cyclic performance at high current density for the Fe_3C-SnO_2@void@C composites were displayed in Fig. 6c. As expected, this anode can provide a good LIB performance with reversible capacities of ~580 mAh g^{-1} after 350 cycles and ~500 mAh g^{-1} after 480 cycles at 800 mA g^{-1}, revealing that the synergistic effect of the SnO_2 active component, carbon protective shell and Fe_3C catalyst can effectively improve their LIB performance. The SEM images from Fig. S8 reveals that the carbon shell structures maintained integrity, which also prove the aforementioned results.

Interestingly, using the TGA result to calculate the reversible capacity (C_{rev}) contribution, C_{rev} for Fe_3C-SnO_2@void@C tested at 200 mA g^{-1} as shown in Fig. 6a, is larger than their theoretical capacity of 782 mAh g^{-1} for SnO_2 corresponding to the highly reversible alloy reaction 2 of "$xLi^+ + Sn + xe^- \leftrightarrow LixSn$ ($0 \le x \le 4.4$), and 425 mAh g^{-1} for Fe_3C modified hollow carbon spheres (Fe_3C-HCS). Some recent reports pointed out that HCS structures could exhibit pseudocapacitive behavior, simultaneously achieving both large power density and high energy output [25,27,28]. Thus, investigating the related redox behavior from capacitive contribution is important to reveal the enhanced mechanism for Fe_3C-SnO_2@void@C anodes.

As previous reported, hollow carbon-coating shell with large specific surface and good conductance could possibly exhibit pseudocapacitive behavior, simultaneously achieving both large power density and high energy output [27,28]. Fig. S9 compares the BET results of the pure SnO_2 and Fe_3C-SnO_2@void@C. The values of specific surface area for Fe_3C-SnO_2@void@C is 199.6 m^2 g^{-1}, being much larger than that of 84.2 m^2 g^{-1} for pure SnO_2 without void carbon shell coating. In addition, the BJH pore size distribution shown in Fig. S8b also shows that 2–10 nm pores/mesopores are in majority for Fe_3C-SnO_2@void@C, but not exist in pure SnO_2. The relatively more pores can store electrolyte, boost the ion transport and effectively contribute the pseudocapacitive capacity, thus ensuring good LIB performance at high currents. As shown in Fig. 7a, CV curves were tested at different sweep rates between 0.5 and 10 mV s^{-1} to analyze the Li^+ storage behavior in Fe_3C-SnO_2@-void@C anode. The current in a scan rate experiment can be

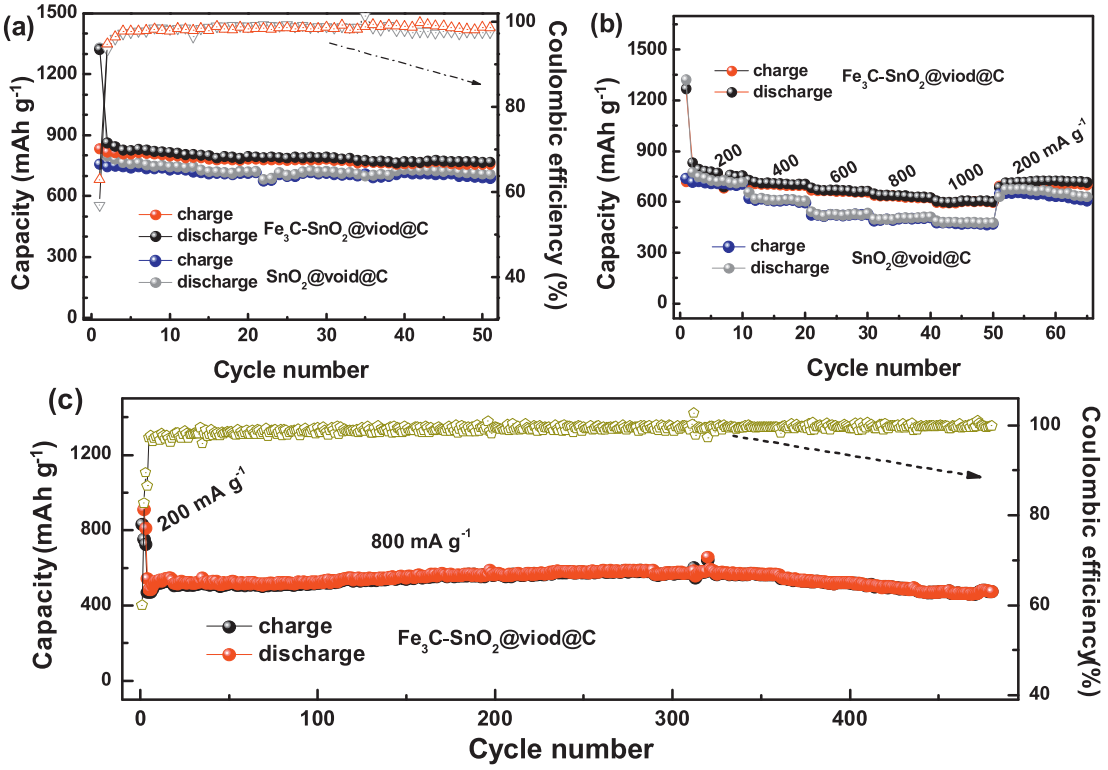

Fig. 6. Cycling performance of SnO_2@void@C and Fe_3C-SnO_2@void@C electrodes at room temperature between 0.05 and 3.00 V: (a) at a current density of 0.2 A g^{-1} and the corresponding Coulombic efficiency; (b) at various current densities from 0.2 A g^{-1} to 1.0 A g^{-1}; (c) long cycling performance of Fe_3C-SnO_2@void@C electrode tested at a high current density of 0.8 A g^{-1}.

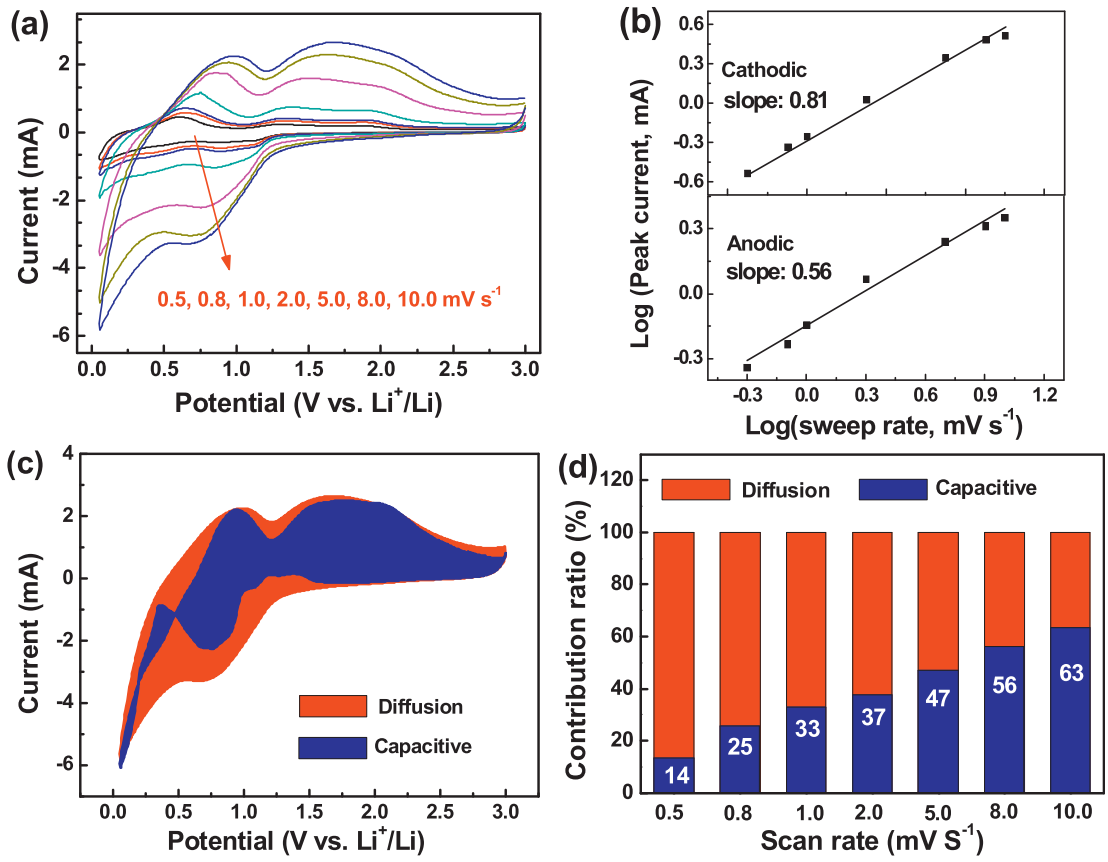

Fig. 7. (a) CV curves of Fe_3C-SnO_2@void@C at various scan rates from 0.5 to 10.0 mV s^{-1}; (b) Specific peak currents at various scan rates from 0.5 to 10.0 mV s^{-1}; (c) CV curve with separation between total current (red line) and capacitive currents (blue regions) at 8.0 mV s^{-1}; (d) Comparison of the capacities of diffusion capacitance and capacitive capacitance at various scan rates from 0.5 to 10.0 mV s^{-1}. (For interpretation of the references to colour in this figure legend, the reader is referred to the Web version of this article.)

expressed by an equation of "$i = a * v^b$", where i is the current, v is the potential scan rate, both a and b are the adjustable parameters [32–34]. Herein, the adjustable coefficient b varied between 0.5 and 1.0, can qualitatively reveal the capacity contributions ratio of a diffusion-limited process and a capacitive process, as pointed out previously [34,35]. The varied Li^+ storage behavior can also be quantified and separated. The fitting value of b being close to 0.5 indicates the dominated diffusion-controlled process, while that near 1.0 implies the full capacitive controlled process [34]. The b-values of the yolk-shell structured Fe_3C-SnO_2@void@C for cathodic peak and anodic peak can be determined to be 0.81 and 0.56 by plotting log i vs. $log\ v$. Correspondingly, Fig. 7b reveals that the values of coefficient b means a large proportion of surface capacitive contribution for Fe_3C-SnO_2@void@C anode. By using the Trasatti's method [33,35], the total capacitive contribution at a given scan rate could be distinguished into the diffusion-controlled fraction ($k_1v^{1/2}$) and capacitor-like current (k_2v) at a fixed potential (V) according to the equation of "$i(V) = k_1v^{1/2} + k_2v$". And the capacitive current $i(V) = k_2v$ could be extracted from the total one with the value of k_2. In general, after conducting these calculations with all corresponding potential dots, one can plot the capacitive area (noted as blue area) as discovered in Fig. 7c taken the sweep rate of 10.0 mV s^{-1} as an example. Combined with the experimental currents noted as red area in Fig. 7c, about 63% of the total capacitances can be calculated. Subsequently, the contribution ratio of capacitance can be obtained and the related histogram is presented in Fig. 7d. Fig. 7d shows that the capacitive contribution ratio obviously increased with increasing the sweep rates, signifying the large rate capacity exists on Fe_3C-SnO_2@void@C materials. Overall, these results can explain that the additional reversible capacities arise from capacitive contribution, as well as reveal the related electrochemical dynamics mechanism for the enhanced LIB performance for Fe_3C-SnO_2@void@C anodes.

4. Conclusions

In summary, a useful strategy has been designed to improve SnO_2 anodes with good electrochemical performance in lithium ion batteries. Fe_3C modification and carbon protective shell with enough reserved space stabilize the SnO_2 anode materials, thereby improving the electrical conductance and the structure stability and thus enhancing the utilization of SnO_2 materials. The prepared composites can deliver good LIB performance with a capacity of ~580 mAh g^{-1} cycling after 350 cycles at 800 mA g^{-1}, good rate capacity, as well as stable cycling life. Based kinetic analysis, it is suggested that the enhanced LIB performance for SnO_2 anodes could be contributed from yolk-shell nanostructure combined with the extra capacity contribution of capacitive lithium absorption. This work supplied an effective method to prepare SnO_2 anodes with good electrochemical performance, and also provide the possible route for other related anode materials.

Acknowledgements

We acknowledge the financial support by the Natural Science Foundations of Fujian Province (Grant No. 2017J01035), the NSF for Distinguished Young Scholars of Fujian Province (Grant No. 2017J07004), the Natural Science Foundations of China (No.

21203025, No. 61574037) and the Strategic Priority Research Program of the Chinese Academy of Sciences (Grant No. XDA09010402).

Appendix A. Supplementary data

Supplementary data to this article can be found online at https://doi.org/10.1016/j.jallcom.2018.12.388.

References

[1] A. Manthiram, X. Yu, S. Wang, Nat. Rev. Mater. 2 (2017) 16103.
[2] X. Zuo, J. Zhu, P. Müller-Buschbaum, Y.-J. Cheng, Nano Energy 31 (2017) 113–143.
[3] X. Ju, H. Huang, W. He, H. Zheng, P. Deng, S. Li, B. Qu, T. Wang, ACS Sustain. Chem. Eng. 6 (2018) 6312–6320.
[4] A.W. Wang, C.D. Wang, L. Fu, Winnie Wong-Ng, Y.C. Lan, Nano-Micro Lett. 9 (2017) 47–69.
[5] X. Ao, J.J. Jiang, Y.J. Ruan, Z.S. Li, Y. Zhang, J.W. Sun, C.D. Wang, J. Power Sources 359 (2017) 340–348.
[6] J.S. Cho, Y.C. Kang, Small 11 (2015) 4673–4681.
[7] J. Abe, K. Takahashi, K. Kawase, Y. Kobayashi, S. Shiratori, ACS Appl. Nano Mater. 1 (2018) 2982–2989.
[8] S. Abouali, M. Akbari Garakani, J.-K. Kim, Electrochim. Acta 284 (2018) 436–443.
[9] H. Li, Q. Su, J. Kang, M. Huang, M. Feng, H. Feng, P. Huang, G. Du, Mater. Lett. 217 (2018) 276–280.
[10] D. Zhou, X. Li, L.-Z. Fan, Y. Deng, Electrochim. Acta 230 (2017) 212–221.
[11] Y. Zhao, J. Li, Y. Ding, L. Guan, RSC Adv. 1 (2011) 852.
[12] D. Zhou, W.-L. Song, X. Li, L.-Z. Fan, Electrochim. Acta 207 (2016) 9–15.
[13] R. Hu, Y. Ouyang, T. Liang, H. Wang, J. Liu, J. Chen, C. Yang, L. Yang, M. Zhu, Adv. Mater. (2017) 29.
[14] J. Cui, S. Yao, J.-Q. Huang, L. Qin, W.G. Chong, Z. Sadighi, J. Huang, Z. Wang, J.-K. Kim, Energy Storage Mater. 9 (2017) 85–95.
[15] Y. Deng, C. Fang, G. Chen, J. Power Sources 304 (2016) 81–101.
[16] D. Zhou, W.-L. Song, L.-Z. Fan, ACS Appl. Mater. Interfaces 7 (2015) 21472–21478.
[17] X. Li, Y. Zhang, H. Zhang, Y. Feng, Y. Wang, Electrochim. Acta 195 (2016) 208–215.
[18] H.Z. Li, L.Y. Yang, J. Liu, S.T. Li, L.B. Fang, Y.K. Lu, H.R. Yang, S.L. Liu, M. Lei, J. Power Sources 324 (2016) 780–787.
[19] Z. Cai, L. Xu, M. Yan, C. Han, L. He, K.M. Hercule, C. Niu, Z. Yuan, W. Xu, L. Qu, K. Zhao, L. Mai, Nano Lett. 15 (2015) 738–744.
[20] D.-S. Kim, H.-W. Shim, M.A. Dar, H. Yoon, H.J. Song, D.-W. Kim, J. Alloys Compd. 769 (2018) 1113–1120.
[21] M. Zou, J. Li, W. Wen, L. Chen, L. Guan, H. Lai, Z. Huang, J. Power Sources 270 (2014) 468–474.
[22] X. Sui, X. Huang, Y. Wu, R. Ren, H. Pu, J. Chang, G. Zhou, S. Mao, J. Chen, ACS Appl. Mater. Interfaces 10 (2018) 26170–26177.
[23] C. Miao, M. Liu, Y.-B. He, X. Qin, L. Tang, B. Huang, R. Li, B. Li, F. Kang, Energy Storage Mater. 3 (2016) 98–105.
[24] Y. Cheng, J. Huang, J. Li, Z. Xu, L. Cao, H. Ouyang, J. Yan, H. Qi, J. Alloys Compd. 658 (2016) 234–240.
[25] M. Zou, L. Wang, J. Li, L. Guan, Z. Huang, Electrochim. Acta 233 (2017) 85–91.
[26] H. Tang, X. Yu, S. Jin, F. Meng, Y. Yan, Z. gao, R. Soc. Open Sci. 5 (2018).
[27] M. Lübke, A. Sumboja, I.D. Johnson, D.J.L. Brett, P.R. Shearing, Z. Liu, J.A. Darr, Electrochim. Acta 192 (2016) 363–369.
[28] H. Yang, R. Xu, Y. Gong, Y. Yao, L. Gu, Y. Yu, Nano Energy 48 (2018) 448–455.
[29] W. Wen, M. Zou, Q. Feng, J. Li, L. Guan, H. Lai, Z. Huang, Electrochim. Acta 182 (2015) 272–279.
[30] W. Luo, X. Ao, Z. Li, L. Lv, J. Li, G. Hong, Q.-H. Wu, C. Wang, Electrochim. Acta 290 (2018) 185–192.
[32] J. Zhang, H. Chen, X. Sun, X. Kang, Y. Zhang, C. Xu, Y. Zhang, J. Electrochem. Soc. 164 (2017) A820–A825.
[33] H. Lindström, S. Södergren, A. Solbrand, H. Rensmo, J. Hjelm, A. Hagfeldt, S.-E. Lindquist, J. Phys. Chem. B 101 (1997) 7717–7722.
[34] X. Xiao, Z. Peng, C. Chen, C. Zhang, M. Beidaghi, Z. Yang, N. Wu, Y. Huang, L. Miao, Y. Gogotsi, J. Zhou, Nano Energy 9 (2014) 355–363.
[35] P. Simon, Y. Gogotsi, B. Dunn, Science 343 (2014) 1210–1211.